Structural Investigations on Octaethylporphyrin Using Density Functional Theory and Polarization-Sensitive Resonance Coherent Anti-Stokes Raman Scattering Spectroscopy

S. Schlücker, J. Koster, M. Nissum,† J. Popp, and W. Kiefer*

Institut für Physikalische Chemie der Universität Würzburg, Am Hubland, D-97074 Würzburg, Germany

Received: June 20, 2001; In Final Form: August 13, 2001

Probing the structure and dynamics of porphyrins by vibrational spectroscopy is of major interest because this cyclic tetrapyrrole system constitutes the chromophore in different very complex biological systems carrying out essential processes in nature such as oxygen transport and storage (hemoglobin and myoglobin, respectively), electron transfer (cytochrome c), and energy conversion (chlorophyll). Most of the biological porphyrins are β-substituted, i.e., substituted at the outer pyrrole carbon atoms. Investigations on the structure of octaethylporphyrin (OEP) using density functional theory (DFT) as well as linear and nonlinear Raman spectroscopic techniques have been performed. The optimized geometry of OEP reveals a centrosymmetric molecule with local D_{2h} symmetry of the porpyhrin macrocycle showing an excellent agreement with the X-ray structure of OEP. The DFT-derived harmonic vibrational wavenumbers together with the corresponding eigenvectors of several low-wavenumber modes and prominent $a_g(D_{2h})$ and $b_{1g}(D_{2h})$ modes of OEP are presented. Resonance Raman (RR) and multiplex polarization-sensitive resonance coherent anti-Stokes Raman scattering (PS RCARS) spectroscopy have been applied to OEP in dichloromethane to obtain complementary vibrational spectroscopic information. The RR spectrum obtained by excitation within the B or Soret bands reveals mainly a_g modes, whereas the corresponding Raman measurements in resonance with the Q bands have been foiled by excessive fluorescence. In the PS RCARS spectra acquired with Q-band excitation, only b_{1g} modes are detected. The different enhancement pattern of this β-substituted free-base porphyrin in comparison with metalloporphyrins (MP) can reasonably be explained in terms of symmetry lowering ($D_{4h} \rightarrow D_{2h}$) supporting the DFT-derived structure.

1. Introduction

Porphyrins have been investigated in great detail using resonance Raman spectroscopy.[1−9] Because of the almost complete vibrational band assignment existing for porphyrins,[10−12] this method provides detailed structural information. Recently, it has been shown for nickel(II)tetraphenylporphyrin (NiTPP) that density functional theory (DFT) predicts quite subtle structural distortions such as porphyrin ruffling.[13] In combination with the DFT−SQM (scaled quantum mechanical) approach,[13−19] detailed connections between the porphyrin structure and its vibrational spectra can be derived. The combination of both ab initio computational and reliable vibrational spectroscopic data seems to become an invaluable tool for an accurate structure determination and an unambiguous normal mode assignment.

A major problem in acquiring resonance Raman (RR) spectra of porphyrins is the occurrence of fluorescence, especially when an excitation wavelength in resonance with the Q bands is applied. The fluorescence problem in RR spectroscopy can be overcome by the use of coherent anti-Stokes Raman scattering (CARS) spectroscopy.[20,21] In this nonlinear Raman spectroscopic technique, a coherent anti-Stokes signal, ω_{CARS}, is generated through a four-wave-mixing process, $\omega_{CARS} = \omega_L + (\omega_L - \omega_S)$, with ω_L and ω_S being the angular frequencies of the pump and Stokes laser, respectively. CARS is generated if the difference $(\omega_L - \omega_S)$ coincides with the angular frequency of a Raman-active mode. Resonance CARS (RCARS) is detected if ω_L matches an electronic absorption of the molecule under investigation. A further enhancement of the RCARS signal is possible due to double or triple resonances, for example, ω_{CARS} also matching an electronic absorption. Because of the dispersion of the refractive index in condensed phase, the corresponding phase-matching condition for the wave vectors, $\vec{k}_{CARS} = \vec{k}_L + (\vec{k}_L - \vec{k}_S)$, has to be fulfilled. Because the signal is coherent and blue-shifted with respect to the pump laser (ω_L), vibrational spectroscopic information on highly fluorescent molecules is achievable.

Apart from Raman spectroscopic techniques, vibrationally resolved fluorescence and phosphorescence spectroscopy has proven to be a valuable tool to investigate highly fluorescent molecules such as porphyrins.[22,23] Because these techniques are carried out in low-temperature matrices, they offer the possibility of studying molecular properties under conditions in which interactions with the environment are minimized. In contrast, Raman and CARS spectroscopies in condensed phase provide information about the molecular symmetry in a solvent environment.

The detectability of species in condensed phase by means of RCARS spectroscopy is strongly limited by the non-Raman-resonant background. The interference of the background with the Raman-resonant CARS signal leads to complex band shapes such as dispersive and negative profiles.[21] However, the background can be suppressed in a polarization-sensitive (PS) or -resolved RCARS experiment.[24−30] At a fixed angle between the pump and Stokes laser, the polarization plane of the non-

---

* To whom correspondence should be addressed. E-mail: wolfgang.kiefer@mail.uni-wuerzburg.de.

† Present address: MWG-Biotech AG, Anzinger Str. 7, D-85560 Ebersberg, Germany.

10.1021/jp012350t CCC: $20.00

Raman-resonant background is well-defined. By the placement of an analyzer perpendicular to this plane, the background can be suppressed resulting in Lorentzian band shapes of the resonant CARS signal. The polarization direction of the Raman-resonant CARS signal itself depends on the depolarization ratio of the corresponding mode. Therefore, specific vibrational porphyrin modes can be selected according to their symmetry by adjusting the analyzer position.[27,30] However, a complicated band analysis due to the interference mentioned above is usually required to identify mode symmetries and vibrational wavenumbers.[27,30] To avoid this fitting procedure to the expression of the third-order nonlinear susceptibility, $\chi^{(3)}$, and to facilitate the spectral interpretation, very high porphyrin concentrations are used.

2. Experimental Section

OEP was purchased from Porphyrin Products (Logan, UT) and used without further purification. Solutions of ~10 mM (for RCARS) and ~1 mM (for RR experiments) in CH_2Cl_2 were used. Dichloromethane has a comparatively small number of vibrational bands in the spectral regions of interest.

Computational Methods. Calculations were performed using DFT with the Becke−Lee−Yang−Parr composite exchange−correlation functional (B3LYP) with the 6-31G(d) basis set as implemented in the Gaussian 98 (revision A.7) program package.[31]

Raman Spectroscopic Techniques. The experimental setup for nanosecond multiplex polarization CARS spectroscopy has been described in detail elsewhere.[32] A narrow-band pump laser (ω_L, Molectron DL 200, DCM-filled) and a broad-band Stokes laser (ω_S, Spectra Physics Quanta Ray PDL 3, DCM/pyridine 1-filled) were pumped synchronously by the third (355 nm) and second (532 nm) harmonic, respectively, of a Q-switched Nd:YAG laser (Spectra Physics Quanta Ray GCR 4, 7 ns, 10 Hz). Broad-band lasing was achieved by placing a high-power laser mirror in front of the dispersive elements of the Stokes laser. Pump (ω_L) and Stokes (ω_S) laser beams were focused on the sample by an achromatic lens at the optimum phase-matching angle. The sample was contained in a square-shaped borosilicate glass capillary from Vitro Dynamics (Rockaway, NJ) with an inner diameter of 200 μm. Polarization directions of ω_L, ω_S, and the generated CARS signal (ω_{CARS}) were determined by means of Glan−Thompson prisms and by introducing a double Fresnel rhombus in the ω_L beam. The CARS signal was collected by an achromatic lens and passed through several apertures for laser stray light and fluorescence rejection. Finally, it was focused on the entrance slit of a double monochromator (Spex 1403, 1800 gratings/mm) and detected by a liquid-N_2-cooled CCD camera (Photometrics SDS 9000) in combination with a commercially available software (Photometrics MAPS V2.0). The entrance slit was kept at ~2 cm^{-1}.

The wavelength arrangement of the laser beams together with the absorption spectrum of OEP dissolved in CH_2Cl_2 is shown in Figure 1. The pump laser wavelength of $\lambda_L = 621$ nm is close to the $Q_x(00)$ absorption band maximum at 620 nm. When the Stokes laser wavelength is tuned to $\lambda_S = 687$ (678) nm, a CARS signal centered at $\lambda_{CARS} = 566$ (573) nm or $\tilde{\nu}_{CARS} \approx 1550$ (1350) cm^{-1}, respectively, very close to the $Q_x(01)$ absorption band maximum at 566 nm, is generated. Because of this double resonance situation, the overall wavelength arrangement leads to a strong resonance enhancement of the CARS process. According to the broad-band profile $\Delta\lambda_S$, a spectral region of at least $\Delta\tilde{\nu}_{CARS} \approx 250$ cm^{-1} was covered. Because of the relatively short exposure times resulting from the use of the scanning multichannel technique (SMT),[33] the formation of photoproducts was avoided. All generated SMT-RCARS spectra of OEP were normalized by division with the corresponding featureless non-Raman-resonant background spectra of carbon tetrachloride acquired under the same conditions.

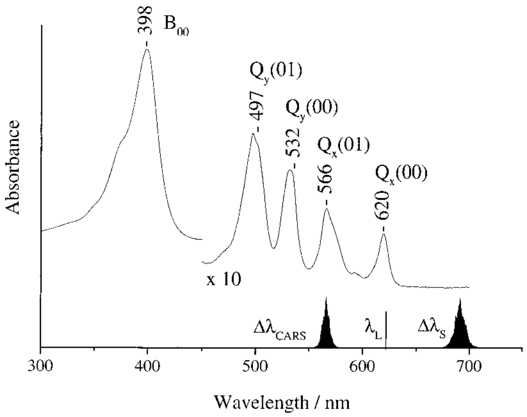

Figure 1. Absorption spectrum of OEP and wavelength arrangement used in the PS RCARS experiments.

For the RR spectra, a dye laser (Spectra Physics 375B) with ~50 mW output power was used. An Ar$^+$ laser (Spectra Physics BeamLok 2085) operating in the UV multimode (~333−364 nm) with an output power of ~3 W was employed as the pump source. The experiments were performed in a conventional 90° scattering geometry. The excitation wavelength was $\lambda_{exc} \approx 423.6$ nm, which is in the vicinity of the maximum of the B or Soret band (Figure 1). The power at the sample was about 5 mW. A rotating cell[34] was used to avoid photodegradation of the sample during the spectra acquisition. The scattered light was collected by a photolens with a very high numerical aperture (Fuji Photo Optical TV lens CF50L with 1:0.7/50) and focused on the entrance slit of a double monochromator (Spex 1404, 2400 gratings/mm). The entrance slit was kept at ~0.7 cm^{-1}. Through the measurement of the spectral lines of potassium vapor around 464 nm, the wavenumber accuracy was estimated to be better than 0.2 cm^{-1}. Sample integrity was monitored spectrophotometrically (Perkin-Elmer Lambda 19) prior to and after both RCARS and RR experiments.

3. Results and Discussion

Density Functional Calculations. The X-ray structure of OEP was determined by Lauher and Ibers in 1973.[35] In this study, a least-squares plane was calculated for the atoms of the porphyrin macrocycle. This portion of the OEP molecule was found to be essentially planar with all atoms within 0.05 Å of the least-squares plane. Besides this nearly D_{2h} local symmetry, a global C_i symmetry of OEP was found. For porphyrin labeling and numbering, see Figure 2.

The experimental values adopted from the X-ray structure were used as an initial guess for the DFT calculations. OEP was constrained to a global C_i symmetry during the geometry optimization. Additionally, the macrocycle and the C_{E_α} atoms were kept in plane yielding a local C_{2h} symmetry. However, the deviations from an ideal D_{2h} symmetry of the macrocyle were negligibly small. The optimized geometry is shown in Figure 3. All calculated vibrational wavenumber values were real. Several low-wavenumber out-of-plane modes were calculated. The first four of them were assigned to porphyrin saddling, ruffling, doming, and waving. The corresponding eigenvectors together with their unscaled harmonic wavenumbers are shown in Figure 4. Because no imaginary wavenumber was calculated

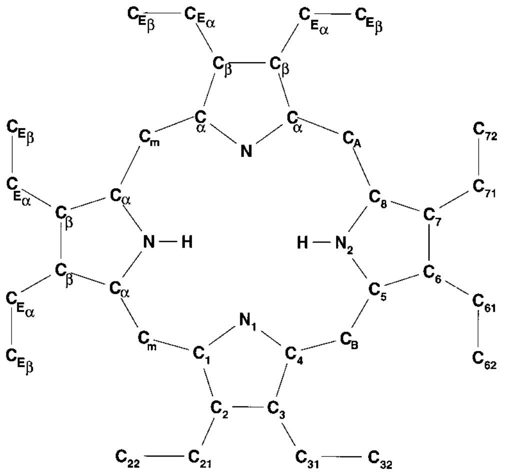

Figure 2. A two-dimensional sketch of the centrosymmetric OEP molecule. The labeling scheme in the upper left half indicates the general positions. The numbering scheme in the lower right is used for specific atoms.

at this level of theory, the energy gain resulting from a distortion of macrocycle planarity is obviously very small.

In the following, a general description of the structural characteristics of OEP as well as a comparison between the experimental and calculated geometry is given. Table 1 shows selected bond distances (in angstroms) and bond angles (in degrees) of OEP from the X-ray study[35] and the geometry optimization at the B3LYP/6-31G(d) level. In general, the values show an excellent agreement. The deviations for the $C_{E_\alpha}-C_{E_\beta}$ bond distances of the ethyl groups are a little bit larger because B3LYP slightly overestimates single bond lengths.[37] The large deviations in the N−H and C_m-H_m distances are attributed to the experimental limitation of X-ray spectroscopy in determining the proton positions accurately. The delocalization of π-electron density throughout the porphyrin macrocycle results in C−C and C−N bond distances that are intermediate between those expected for single and for double bonds. The bond lengths are comparable to values found for similar bonds in aromatic systems. The protonated and deprotonated pyrrole rings in the centrosymmetric OEP molecule differ slightly. Both the $C_\alpha-C_\beta$ and the $C_\beta-C_\beta$ bond distances in each of the pyrrole rings are increased by about 0.01 Å in OEP compared to those in the unsubstituted porphine molecule. This bond elongation indicates a reduction in the π-electron density at the substituted C_β atoms and a subsequent transfer of π-electron density to the substituent atoms. Consequently, the average $C_\beta-C_{E_\alpha}$ bond lengths are shortened in comparison to a regular C−C single bond (∼154 pm).

Resonance Raman Spectroscopy. The RR spectrum of OEP was obtained with 423.6 nm excitation. Although the excitation wavelength does not coincide with the maximum absorption of the B or Soret-band at 398 nm (Figure 1), a_g modes are still strongly resonance enhanced. Sato et al.[36] made extensive studies on the S_0, S_1, and T_1 species of OEP. Their band assignment was ensured by a detailed analysis of the RR spectra of several OEP isotopomers. The RR spectrum in the wavenumber region 1100−1700 cm^{-1} presented in Figure 5 closely resembles the resonance enhancement features observed by Sato et al. under similar conditions. The corresponding band assignment is listed in Table 2. In agreement with the RR spectrum of MgOEP, the band at 1423 cm^{-1} is assigned to a CH_2 scissoring mode.[38] As proposed earlier, the very strong band at 1370 cm^{-1} is due to a Fermi resonance between ν_4 and the first overtone of ν_7 since this band splits up into two bands upon meso deuteration.[36] In the case of NiOEP,[11] the very strong enhancement for the mode ν_4 was explained by comparing the porphyrin ν_4 eigenvector with the corresponding LUMO of the Soret transition. The ν_4 eigenvector is especially well-matched to the bonding change associated with the electronic transition.[11] The single band at 1126 cm^{-1} reported by Sato et al.[36] is resolved into two bands at 1120 and 1132 cm^{-1} (Figure 5). In accordance with the reported sensitivity toward d_{28}-substitution[36] and RR data taken from NiOEP ($\tilde{\nu}_5 = 1138$ cm^{-1}, $\tilde{\nu}_{14} = 1131$ cm^{-1}), these bands are assigned to ν_{14} and ν_5, respectively.[11]

In Figures 6 and 7, the eigenvectors of several prominent Raman-active normal modes of OEP together with the calculated harmonic wavenumbers and the experimental values from the RR spectrum (Figure 5 and Table 2) are shown. In general, the calculated harmonic wavenumbers overestimate the experimental values by about 30−50 cm^{-1}, which is in good agreement for this level of theory without applying a scaling procedure to

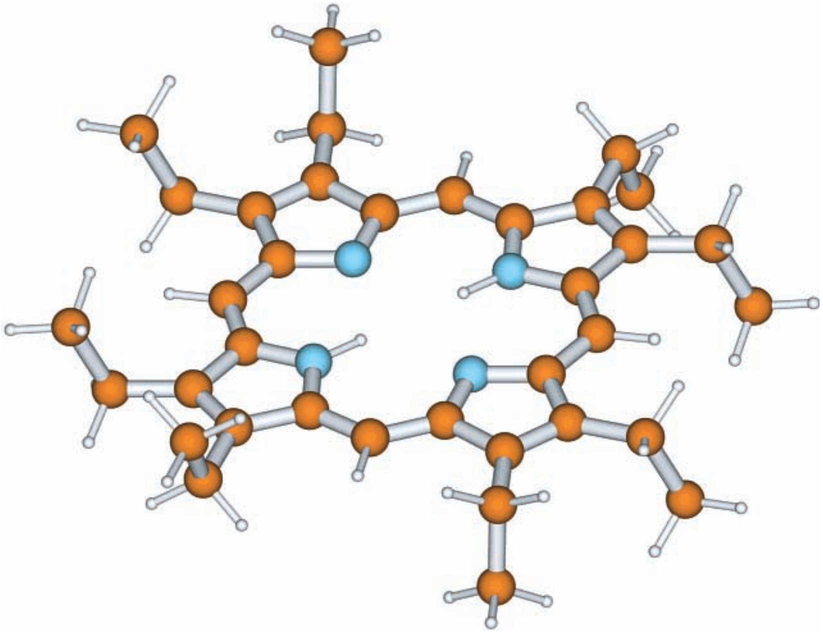

Figure 3. Geometry of OEP optimized at the B3LYP/6-31G(d) level (C_i-constraints).

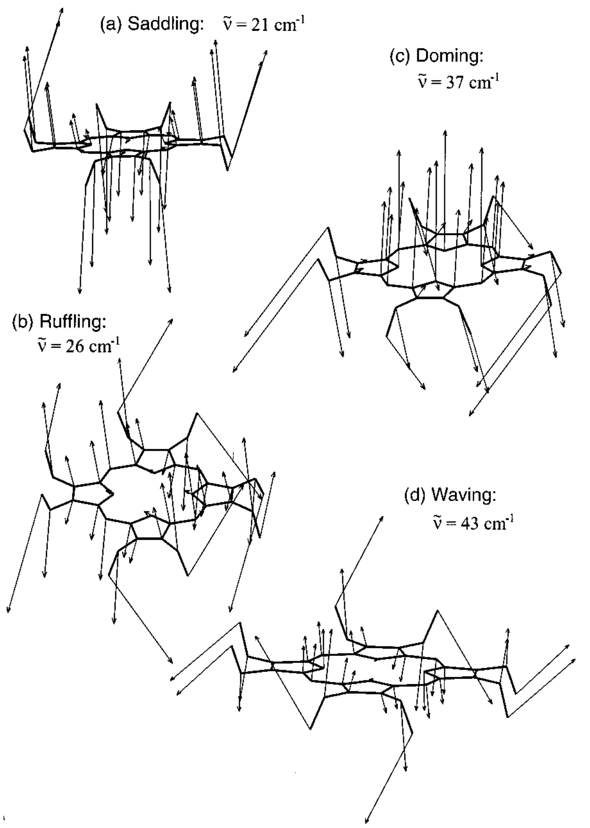

Figure 4. Eigenvectors and calculated harmonic wavenumbers (unscaled values) of the first four low-wavenumber (out-of-plane) modes of OEP showing distinct distortions of the porphyrin macrocycle: (a) saddling, (b) ruffling, (c) doming, and (d) waving. Protonated (pyrrole-like) rings are aligned horizontally; deprotonated (pyrrolenine-like) rings are aligned vertically.

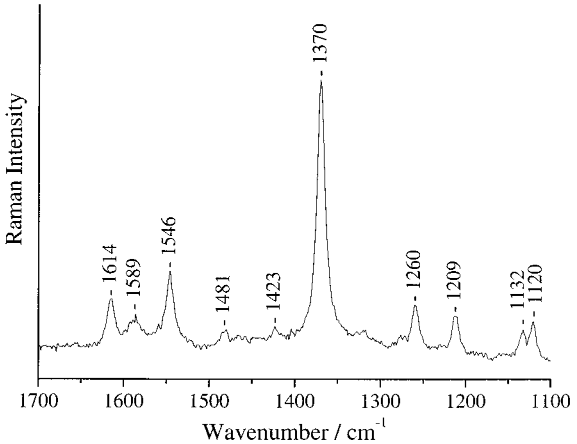

Figure 5. Resonance Raman spectrum of OEP in the range of 1100−1700 cm^{-1} obtained with 423.6 nm excitation.

TABLE 1: Selected Bond Distances (Å) and Angles (deg) of OEP[a]

Deprotonated Pyrrole Rings

	exptl	calcd		exptl	calcd
N_1-C_1	1.3639	1.3619	$C_1-N_1-C_4$	105.7	105.4
N_1-C_4	1.3635	1.3618	$N_1-C_1-C_2$	110.9	111.5
C_1-C_2	1.4614	1.4699	$N_1-C_4-C_3$	110.8	111.5
C_3-C_4	1.4638	1.4700	$C_1-C_2-C_3$	106.3	105.8
C_2-C_3	1.3535	1.3663	$C_4-C_3-C_2$	106.3	105.8
$C_1-C_{B'}$	1.3936	1.4005	$N_1-C_1-C_{B'}$	125.0	125.0
C_4-C_B	1.3930	1.4005	$N_1-C_4-C_B$	125.2	125.0
C_2-C_{21}	1.5006	1.5033	$C_3-C_4-C_B$	123.9	123.4
C_3-C_{31}	1.4940	1.5033	$C_2-C_1-C_{B'}$	124.1	123.5
$C_{21}-C_{22}$	1.5143	1.5417	$C_1-C_2-C_{21}$	125.7	125.8
$C_{31}-C_{32}$	1.5231	1.5417	$C_4-C_3-C_{31}$	125.7	125.8
			$C_3-C_2-C_{21}$	127.9	128.4
			$C_2-C_3-C_{31}$	128.0	128.5
			$C_2-C_{21}-C_{22}$	114.4	113.7
			$C_3-C_{31}-C_{32}$	112.8	113.7

Protonated Pyrrole Rings

	exptl	calcd		exptl	calcd
N_2-C_5	1.3660	1.3705	$C_5-N_2-C_8$	109.6	110.7
N_2-C_8	1.3679	1.3705	$C_5-N_2-(N_2-H)$	124.8	124.7
$N_2-(N_2-H)$	0.918	1.015	$C_8-N_2-(N_2-H)$	125.5	124.6
C_5-C_6	1.4383	1.4439	$N_2-C_5-C_6$	107.7	107.0
C_7-C_8	1.4380	1.4439	$N_2-C_8-C_7$	107.8	107.0
C_6-C_7	1.3729	1.3832	$C_5-C_6-C_7$	107.5	107.6
C_5-C_B	1.3919	1.3937	$C_8-C_7-C_6$	107.3	107.6
C_8-C_A	1.3884	1.3937	$N_2-C_5-C_B$	125.0	125.3
C_6-C_{61}	1.4987	1.5038	$N_2-C_8-C_A$	124.5	125.3
C_7-C_{71}	1.4964	1.5038	$C_6-C_5-C_B$	127.3	127.7
$C_{61}-C_{62}$	1.5221	1.5414	$C_7-C_8-C_A$	127.3	127.7
$C_{71}-C_{72}$	1.5216	1.5413	$C_5-C_6-C_{61}$	124.9	124.5
			$C_8-C_7-C_{71}$	125.0	124.5
			$C_7-C_6-C_{61}$	127.6	127.9
			$C_6-C_7-C_{71}$	127.7	127.9
			$C_6-C_{61}-C_{62}$	112.9	113.7
			$C_7-C_{71}-C_{72}$	113.1	113.7
$C_A-(C_A-H)$	1.000	1.0849	$C_4-C_B-C_5$	127.4	127.8
$C_B-(C_B-H)$	0.956	1.0849	$C_1-C_{B'}-C_\alpha$	127.7	127.7
			$(C_B-H)-C_B-C_4$	117.4	116.7
			$(C_{B'}-H)-C_{B'}-C_1$	116.9	116.7
			$(C_B-H)-C_B-C_5$	115.1	115.5
			$(C_{B'}-H)-C_{B'}-C_\alpha$	115.3	115.5

[a] Experimental values adopted from Lauher and Ibers.[35] Theoretical values calculated at the B3LYP/6-31G(d) level (C_i-constraints).

account for anharmonicity effects. Except for Figure 7c, only the carbon skeleton (carbon atoms of the macrocycle and the ethyl side chains) is indicated by bold lines in Figures 6 and 7. Protonated (or pyrrole-like) rings are aligned horizontally; deprotonated (or pyrrolenine-like) rings are aligned vertically. For a centrosymmetric molecule such as OEP, normal modes are either allowed in the IR spectrum (ungerade modes) or allowed in the Raman spectrum (gerade modes) but not allowed in both because of the well-known exclusion principle. All normal modes presented in Figures 6 and 7 are Raman active (a_g modes in C_i point group). The symmetry of normal modes given in brackets in Table 2 refers only to the porphyrin macrocycle because OEP, to a very close approximation, has a local D_{2h} symmetry (compare Table 1). Except for two modes [$\nu_{19}(b_{1g})$, Figure 6b and $\nu_{28}(b_{1g})$, Figure 7a], only $a_g(D_{2h})$ modes are shown. Figure 6a shows the eigenvectors of the normal mode ν_{10}. The main amplitude of this asymmetric $C_\alpha C_m$ stretching mode is localized on the $C_\alpha C_m C_\alpha$ triatom bridge coupled with a strong $C_\beta C_\beta$ stretching component for the deprotonated pyrrole rings. The normal mode ν_{19} (Figure 6b) is also an asymmetric $C_\alpha C_m$ stretching mode for which the $C_\alpha C_m$ bonds connected to the protonated rings possess much larger amplitudes than those connected to the deprotonated rings. Both of the normal modes ν_2 and ν_{11} (Figure 6c,d) are $C_\beta C_\beta$ stretching modes. For the ν_2, the $C_\beta C_\beta$ stretching components on protonated and deprotonated rings (larger amplitudes) are in-phase, whereas for the ν_{11} they are out-of-phase (with larger amplitudes for the protonated rings). Figure 7a shows the symmetric $C_\alpha C_m$ stretching mode ν_{28} having larger amplitudes for the $C_\alpha C_m$ bonds attached to deprotonated rings. The normal mode ν_4 (Figure 7b) is a symmetric pyrrole half-ring mode (same phase for both $N-C_\alpha$ bonds, alternate sign for both $C_\alpha C_\beta$ bonds and, therefore, phase alternations between $N-C_\alpha$ and $C_\alpha C_\beta$ bonds) with the eigenvectors on protonated and deprotonated rings in-phase. In Figure

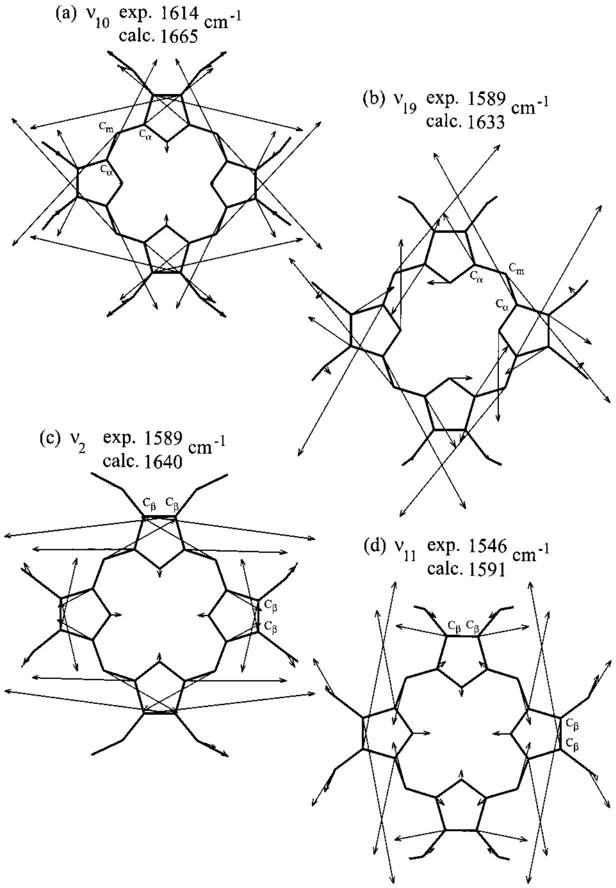

Figure 6. Eigenvectors and calculated harmonic wavenumbers (unscaled values) of several prominent Raman-active OEP normal modes together with the corresponding experimental values (wavenumber region, 1540−1620 cm^{-1}) taken from the RR spectrum (Figure 5, Table 2): (a) ν_{10}, $\nu(C_\alpha C_m)_{asym}$; (b) ν_{19}, $\nu(C_\alpha C_m)_{asym}$; (c) ν_2, $\nu(C_\beta C_\beta)$; (d) ν_{11}, $\nu(C_\beta C_\beta)$. Protonated (pyrrole-like) rings are aligned horizontally; deprotonated (pyrrolenine-like) rings are aligned vertically.

TABLE 2: Band Assignment for the RR Spectrum of OEP Obtained with 423.6 nm Excitation

$\tilde{\nu}$, cm^{-1}	ν_i (sym, D_{2h})	description
1614	ν_{10} (a$_g$)	$\nu(C_\alpha-C_m)_{asym}$
1589	ν_{19} (b$_{1g}$), ν_2(a$_g$)	$\nu(C_\alpha-C_m)_{asym}$, $\nu(C_\beta-C_\beta)$
1546	ν_{11} (a$_g$)	$\nu(C_\beta-C_\beta)$
1481	ν_{28} (b$_{1g}$)	$\nu(C_\alpha-C_m)_{sym}$
1423		CH$_2$ scissoring
1370	ν_4 (a$_g$), 2ν_7 (a$_g$)	ν(Pyr half-ring)$_{sym}$, δ(Pyr def)$_{sym}$
1260		CH$_2$ twist
1209	ν_{13} (a$_g$)	$\delta(C_m-H)$
1132	ν_5 (a$_g$)	$\nu(C_\beta-C_1)_{sym}$
1120	ν_{14} (a$_g$)	$\nu(C_\beta-C_1)_{sym}$

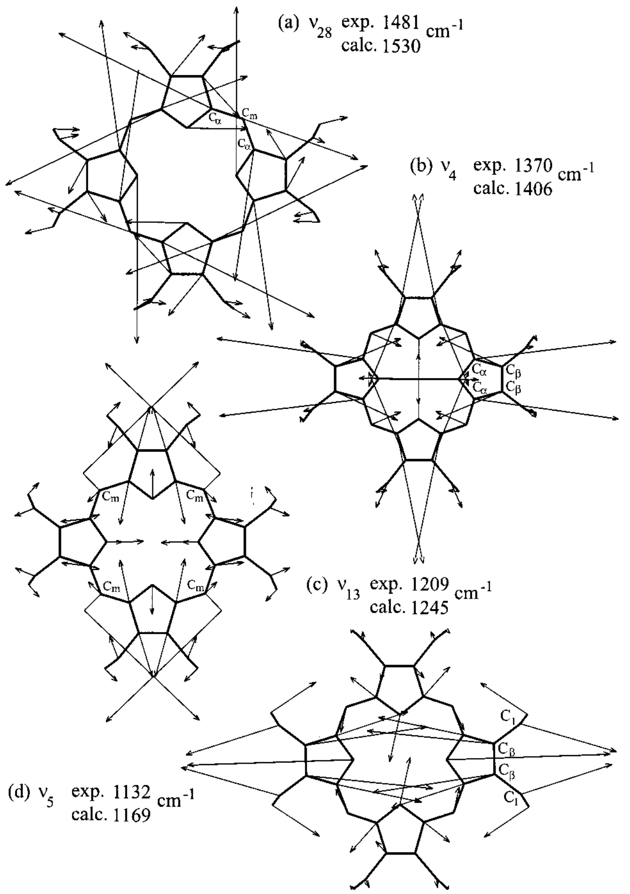

Figure 7. Eigenvectors and calculated harmonic wavenumbers (unscaled values) of several prominent Raman-active OEP normal modes together with the corresponding experimental values (wavenumber region, 1130−1490 cm^{-1}) taken from the RR spectrum (Figure 5, Table 2): (a) ν_{28}, $\nu(C_\alpha C_m)_{sym}$; (b) ν_4, ν(Pyr half-ring)$_{sym}$; (c) ν_{13}, $\delta(C_mH)$; (d) ν_5, $\nu(C_\beta C_1)_{sym}$. Protonated (pyrrole-like) rings are aligned horizontally; deprotonated (pyrrolenine-like) rings are aligned vertically.

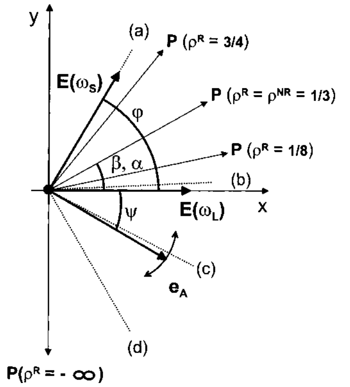

Figure 8. Polarization vectors in the PS RCARS experiment. All angles (α, β, φ, and ψ) are defined with respect to the x-axis. The x-axis is aligned parallel with the unit polarization vector of the pump laser ($\mathbf{E}(\omega_L)$). The Stokes laser polarization ($\mathbf{E}(\omega_S)$), the polarization of the non-Raman-resonant background ($\mathbf{P}^{NR}$) and the Raman-resonant CARS signal ($\mathbf{P}^{R}$) form angles of $\varphi = 60°$, α, and β with the pump laser polarization, respectively. The dotted lines numbered a−d indicate the analyzer positions, ψ, for which the spectra in Figure 9 were acquired.

7c, the eigenvectors for the C$_m$H deformation mode ν_{13} coupled with strong CH$_2$ twistings of the ethyl side chains are shown. The eigenvectors of the symmetric C$_\beta$C$_1$ stretching mode coupled with the ring coordinates shown in Figure 7d are mainly localized on the protonated rings, and therefore, this mode was assigned to ν_5. In contrast, the symmetric C$_\beta$C$_1$ stretching mode ν_{14} (not shown) is mainly localized on deprotonated rings. In summary, the normal mode pattern is found to resemble that of porphine (H$_2$P)[12] and NiOEP[11].

Polarization-Sensitive CARS Spectroscopy. PS RCARS experiments were performed in accordance with Voroshilov et al.[30] with an angle of $\varphi = 60°$ between the pump, $\mathbf{E}(\omega_L)$, and Stokes laser, $\mathbf{E}(\omega_S)$, polarization directions (Figure 8). Depolarization ratios in CARS spectroscopy are defined as[21,25]

$$\rho^{R,NR} = \frac{\chi^{(3)R,NR}_{1221}}{\chi^{(3)R,NR}_{1111}} \tag{1}$$

for the Raman-resonant CARS signal (ρ^R) and the non-Raman-resonant background (ρ^{NR}). In the case of a wavenumber

TABLE 3: Symmetry Correlation between D_{4h} and D_{2h} Point Groups for Raman Active In-plane Modes

D_{4h}	$\rho(D_{4h})$	D_{2h}	$\rho(D_{2h})$
a_{1g}	$^1/_8$	a_g	$^1/_8 < \rho < {^3/_4}$
b_{1g}	$^3/_4$	same as a_g	
a_{2g}	∞	b_{1g}	$^3/_4 < \rho < \infty$
b_{2g}	$^3/_4$	same as b_{1g}	

degenerate CARS experiment performed in an isotropic medium, $\chi^{(3)}_{1111}$ and $\chi^{(3)}_{1221}$ represent the two independent components of the third-order nonlinear susceptibility tensor that can be distinguished. It is assumed that ρ^{R} and ρ^{NR} have real values and that the Raman-resonant CARS signal $\mathbf{P}^{R}$ and the non-Raman-resonant background $\mathbf{P}^{NR}$ are linearly polarized. The polarization directions of $\mathbf{P}^{R}$ and $\mathbf{P}^{NR}$ form angles β and α with $\mathbf{E}(\omega_L)$, given by[24,25]

$$\tan\beta = \rho_R \tan\varphi \qquad (2)$$

$$\tan\alpha = \rho_{NR} \tan\varphi \qquad (3)$$

Through the introduction of an analyzer in the CARS signal beam, specific contributions of different polarizations can be selected. The analyzer forms an angle, ψ, with the pump laser ($\mathbf{E}(\omega_L)$) beam (Figure 8). According to eq 2, specific Raman modes can be selected because of their corresponding depolarization ratios, ρ_R. In an optically transparent and isotropic medium, the value of $\rho_{NR} = {^1/_3}$ is given in particular (see Figure 8). Background-free spectra are obtained by positioning the analyzer perpendicular to the direction of ρ_{NR}, i.e., at $\psi = \alpha - 90° = -60°$. This analyzer position (d) is indicated by a dotted line in Figure 8.

Specific porphyrin mode symmetries can be selected according to eq 2. In metalloporphyrins with D_{4h} symmetry, the dominant allowed Raman modes under resonance conditions possess a_{1g}, b_{1g}, a_{2g}, or b_{2g} symmetry[1] with depolarization ratios of $\rho^{R} = {^1/_8}, {^3/_4}, \infty$, and $^3/_4$, respectively.[30,39] The corresponding polarization directions calculated from eq 2 are given by $\varphi = 12.2°, 52.4°, -90°$, and $52.4°$, respectively (Figure 8). The symmetry correlation between the D_{4h} and D_{2h} point group is given in Table 3. Considering the change from metalloporphyrins (D_{4h}) to free-base porphyrins (D_{2h}) as a perturbation,[12] only small changes in depolarization ratios are expected.

PS RCARS spectra of OEP were carried out at a pump laser wavelength of 621 nm in resonance with the $Q_x(00)$ band (Figure 1). Measurements in the region 1250−1650 cm^{-1} were performed at the four different analyzer positions (a)−(d) indicated as dotted lines in Figure 8. The corresponding PS RCARS spectra are shown in Figure 9.

In metalloporphyrins (D_{4h}), primarily modes with b_{1g}, b_{2g}, and a_{2g} symmetry are enhanced under Q-band resonance conditions.[1] The b_{1g} species (D_{4h}) corresponds to the a_g representation in free-base porphyrins (D_{2h}, see Table 3). These modes are enhanced with B or Soret-band excitation. Only b_{1g} (D_{2h}) modes in free-base porphyrins, correlated to the b_{2g} and a_{2g} species (Table 3) in metalloporphyrins (D_{4h}), are enhanced under Q band resonance conditions.

At analyzer position a with $\psi = +60°$ (Figures 8 and 9, spectrum a), modes with $\rho^{R} = {^3/_4}$ are selected and show their maximum absolute intensity. Strong contributions from the non-Raman-resonant background ($\rho^{NR} = {^1/_3}$) reduce the signal-to-noise ratio. The polarization behavior of the mode ν_{19} (b_{1g}) at 1588 cm^{-1} at different analyzer positions, a−d, shall be explained explicitly. At analyzer position b with $\psi = +2°$ (Figures 5 and 6, spectrum b), its signal intensity is drastically reduced. The spectrum is dominated by the non-Raman-resonant background, and almost no contributions from ν_{19} (b_{1g}) are detectable. When the analyzer plane is turned further to position c with $\psi = -28°$ (Figures 8 and 9, spectrum c), the contribution of the background is reduced. The analyzer is only 10° off the perfect crossing angle of the polarization plane of modes with $\rho^{R} = {^3/_4}$. Nevertheless, some signal intensity is detectable indicating an anomalous polarization of ν_{19} ($^3/_4 < \rho < \infty$). For the RR spectrum upon excitation at 504 nm close to the $Q_y(01)$ absorption of OEP, it was reported that anomalously polarized (ap) bands are strongly enhanced, similar to the inversely polarized (ip) bands of metalloporphyrins (MP).[36] The different polarization properties can reasonably be explained in terms of symmetry lowering. For these modes, the polarizability tensor[39] is antisymmetric for metalloporphyrins (D_{4h}) but asymmetric for free-base porphyrins (D_{2h}). At analyzer position d with $\psi = -60°$ (Figures 8 and 9, spectrum d), the non-Raman-resonant background is completely suppressed. At this angle, ν_{19} shows its maximum RCARS intensity relative to the background. The elimination of the background produces Lorentzian band shapes.[21] The mode at 1538 cm^{-1} is assigned to ν_{19} in the lowest excited singlet state (S_1, $^1(\pi\pi^*)$) of OEP, reported at 1534 cm^{-1} by Sato et al.,[36] because it closely resembles the polarization behavior of $\nu_{19}(S_0)$. In contrast, no Raman bands for the corresponding triplet species in close vicinity of this wavenumber value were reported.[36] A further argument confirming this assignment is the fact that with an increasing pump and Stokes laser power the intensity ratio $\nu_{19}(S_1)/\nu_{19}(S_0)$ increases, too.

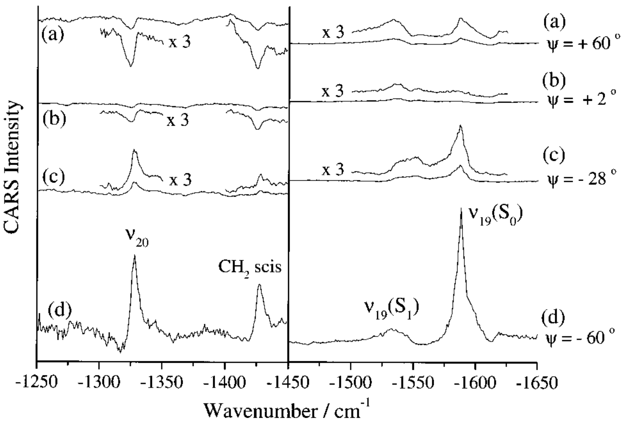

Figure 9. Polarization-sensitive resonance CARS spectra of OEP in the range −1250 to −1650 cm^{-1} obtained at different analyzer positions, ψ.

In the wavenumber region 1250−1450 cm^{-1}, two bands exhibiting dispersive band shapes (Figure 9, spectrum b) and negative Lorentzian profiles (Figure 9, spectrum a) are observable. These complex band shapes arise from the interference of the non-Raman-resonant background of the solvent and the RCARS signal of OEP. When the analyzer is turned from $\psi = -28°$ to $\psi = -60°$ (Figure 8, spectra c and d), an efficient suppression of the background is achieved. The band at 1423 cm^{-1} is assigned to a CH_2 scisscoring mode with b_{1g} symmetry. The band at 1327 cm^{-1} is assigned to ν_{20} (b_{1g}). Similar to ν_{10} (b_{1g}), it was reported[36] that ν_{20} is anomalously polarized upon excitation at 504 nm.

In the PS RCARS spectra of MgOEP, for example, the modes ν_{10} and ν_{11} were reported.[38] The irreducible representation b_{1g} in D_{4h} corresponds to the species a_g in D_{2h} (Table 3). Consequently, these modes are not enhanced under Q-band resonance conditions for OEP and therefore not observed.

However, the modes ν_{19} and ν_{20} were detected in the PS RCARS spectra of both MgOEP and OEP. Because these modes have a_{2g} (D_{4h}) or b_{1g} (D_{2h}) symmetry, respectively, they are enhanced with Q-band excitation. In summary, these results strongly indicate a D_{2h} symmetry of the OEP macrocycle.

4. Conclusions

Structure investigations on OEP have been performed using DFT and Raman spectroscopy. The DFT calculations on OEP performed at the B3LYP/6-31G(d) level closely resemble the characteristic features of the X-ray structure. Several calculated low-wavenumber out-of-plane modes are assigned to porphyrin saddling, ruffling, doming, and waving according to their eigenvectors. The energy gain resulting from a distortion of macrocycle planarity is obviously very small because no imaginary wavenumber was calculated at this level of theory. The eigenvectors of several prominent Raman-active OEP normal modes together with their calculated harmonic wavenumbers are presented, and the normal mode pattern is found to resemble that of porphine (H_2P) and NiOEP. RR spectroscopy with excitation in the B-band or Soret band and PS RCARS spectroscopy under Q-band resonance conditions yield complementary vibrational spectroscopic information. In contrast to metalloporphyrins (D_{4h}) such as MgOEP, for which a_{2g}, b_{1g}, and b_{2g} modes have been observed in the PS RCARS spectrum with Q-band excitation, only b_{1g} modes were found for OEP (D_{2h}). The different enhancement pattern due to symmetry lowering ($D_{4h} \rightarrow D_{2h}$) is confirmed by the RR spectrum under B-band or Soret-band excitation, in which mainly a_g modes are observed. In summary, the combination of DFT calculations and Raman spectroscopy under various resonance conditions is regarded as a powerful tool to achieve structural information on highly fluorescent free-base porphyrins and metalloporphyrins. Ongoing studies using this methodology focus on symmetrically and unsymmetrically β-substituted free-base porphyrins with larger relevance in biology than the synthetic and highly symmetrically substituted OEP.

Acknowledgment. Support from the Deutsche Forschungsgemeinschaft (Sonderforschungsbereich 347) and the Fonds der Chemischen Industrie is highly acknowledged. S. Schlücker is grateful to the Stipendienfonds im Fonds der Chemischen Industrie and the Bundesministerium für Bildung und Forschung for a postgraduate fellowship. J. Popp gratefully acknowledges support from the Freistaat Bayern (Bayerisches Habilitationsförderstipendium).

References and Notes

(1) Spiro, T. G. *Adv. Protein Chem.* **1985**, *37*, 111−159.

(2) Schick, G. A.; Bocian, D. F. *Biochim. Biophys. Acta* **1987**, *895*, 127−154.

(3) Schweitzer-Stenner, R. *Q. Rev. Biophys.* **1989**, *22*, 381−479.

(4) Spiro, T. G.; Czernuszewicz, R. S.; Li, X. Y. *Coord. Chem. Rev.* **1990**, *100*, 541−571.

(5) Spiro, T. G.; Smulevich, G.; Su, C. *Biochemistry* **1990**, *29*, 4497−4508.

(6) Smulevich, G. In *Biomolecular Spectroscopy*; Clark, R. J. H., Hester, R. E., Eds.; Advances in Spectroscopy, Vol. 20; Wiley: Chichester, U.K., 1993; pp 153−193.

(7) Kitagawa, T.; Mizutani, Y. *Coord. Chem. Rev.* **1994**, *135/136*, 685−735.

(8) Spiro, T. G.; Czernuszewicz, R. S. *Methods Enzymol.* **1995**, *246*, 416−460.

(9) Shelnutt, J. A.; Song, X.-Z.; Ma, J.-G.; Jia, S.-L.; Jentzen, W.; Medforth, C. J. *Chem. Soc. Rev.* **1998**, *27*, 31−42.

(10) Li, X.-Y.; Czernuszewicz, R. S.; Kincaid, J. R.; Su, Y. O.; Spiro, T. G. *J. Phys. Chem.* **1990**, *94*, 31−47.

(11) Li, X.-Y.; Czernuszewicz, R. S.; Kincaid, J. R.; Stein, P.; Spiro, T. G. *J. Phys. Chem.* **1990**, *94*, 47−61.

(12) Li, X.-Y.; Zgierski, M. Z. *J. Phys. Chem.* **1991**, *95*, 4268−4287.

(13) Rush, T. S., III; Kozlowski, P. M.; Piffat, C. A.; Kumble, R.; Zgierski, M. Z.; Spiro, T. G. *J. Phys. Chem. B* **2000**, *104*, 5020−5034.

(14) Pulay, P.; Fogarasi, G.; Pongor, G.; Boggs, J. E.; Vargha, A. *J. Am. Chem. Soc.* **1983**, *105*, 7073−7047.

(15) Kozlowski, P. M.; Zgierski, M. Z.; Pulay, P. *Chem. Phys. Lett.* **1995**, *247*, 379−385.

(16) Kozlowski, P. M.; Jarzecki, A. A.; Pulay, P. *J. Phys. Chem.* **1996**, *100*, 7007−7013.

(17) Kozlowski, P. M.; Jarzecki, A. A.; Pulay, P.; Li, X.-Y.; Zgierski, M. Z. *J. Phys. Chem.* **1996**, *100*, 13985−13992.

(18) Spiro, T. G.; Kozlowski, P. M.; Zgierski, M. Z. *J. Raman Spectrosc.* **1998**, *29*, 869−879.

(19) Kozlowski, P. M.; Rush, T. S., III; Jarzecki, A. A.; Zgierski, M. Z.; Chase, B.; Piffat, C.; Ye, B.-H.; Li, X.-Y.; Pulay, P.; Spiro, T. G. *J. Phys. Chem. A* **1999**, *103*, 1357−1366.

(20) Kiefer, W.; Long, D. A. *Nonlinear Raman spectroscopy and its chemical applications*; D. Reidel: Dordrecht, Netherlands, 1982; pp 83−140, 241−470.

(21) Maeda, S.; Kamisuki, T.; Adachi, Y. In *Advances in Nonlinear Raman Spectroscopy.*; Clark, R. J. H., Hester, R. E., Eds.; Advances in Spectroscopy, Vol. 15; Wiley: Chichester, U.K., 1993; pp 253−297.

(22) Radziszewski, J. G.; Waluk, J.; Nepraš, M.; Michl, J. *J. Phys. Chem.* **1991**, *95*, 1963−1969.

(23) Starukhin, A.; Shulga, A.; Waluk, J. *Chem. Phys. Lett.* **1997**, *272*, 405−411.

(24) Brakel, R.; Mudogo, V.; Schneider, F. W. *J. Chem. Phys.* **1986**, *84*, 2451−2458.

(25) Brakel, R.; Schneider, F. W. In *Advances in Nonlinear Raman Spectroscopy*; Clark, R. J. H., Hester, R. E., Eds.; Advances in Spectroscopy, Vol. 15; Wiley: Chichester, U.K., 1993; pp 149−192.

(26) Apanasevich, P. A.; Kvach, V. V.; Orlovich, V. A. *J. Raman Spectrosc.* **1989**, *20*, 125−133.

(27) de Boeij, W. P.; Lucassen, G. W.; Otto, C.; Greve, J. *J. Raman Spectrosc.* **1993**, *24*, 383−396.

(28) Toleutaev, B. N.; Tahara, T.; Hamaguchi, H. *Appl. Phys. B* **1994**, *59*, 369−375.

(29) Kruglik, S. G.; Apanasevich, P. A.; Chrivony, V. S.; Kvach, V. V.; Orlovich, V. A. *J. Phys. Chem.* **1995**, *99*, 2978−2995.

(30) Voroshilov, A.; Otto, C.; Greve, J. *J. Chem. Phys.* **1997**, *106*, 2589−2598.

(31) Frisch, M. J.; Trucks, G. W.; Schlegel, H. B.; Scuseria, G. E.; Robb, M. A.; Cheeseman, J. R.; Zakrzewski, V. G.; Montgomery, J. A., Jr.; Stratmann, R. E.; Burant, J. C.; Dapprich, S.; Millam, J. M.; Daniels, A. D.; Kudin, K. N.; Strain, M. C.; Farkas, O.; Tomasi, J.; Barone, V.; Cossi, M.; Cammi, R.; Mennucci, B.; Pomelli, C.; Adamo, C.; Clifford, S.; Ochterski, J.; Petersson, G. A.; Ayala, P. Y.; Cui, Q.; Morokuma, K.; Malick, D. K.; Rabuck, A. D.; Raghavachari, K.; Foresman, J. B.; Cioslowski, J.; Ortiz, J. V.; Stefanov, B. B.; Liu, G.; Liashenko, A.; Piskorz, P.; Komaromi, I.; Gomperts, R.; Martin, R. L.; Fox, D. J.; Keith, T.; Al-Laham, M. A.; Peng, C. Y.; Nanayakkara, A.; Gonzalez, C.; Challacombe, M.; Gill, P. M. W.; Johnson, B. G.; Chen, W.; Wong, M. W.; Andres, J. L.; Head-Gordon, M.; Replogle, E. S.; Pople, J. A. *Gaussian 98*, revision A.7; Gaussian, Inc.: Pittsburgh, PA, 1998.

(32) Funk, J.-M.; Michelis, T.; Eck, R.; Materny, A. *Appl. Spectrosc.* **1998**, *52*, 1541−1553.

(33) Knoll, P.; Singer, R.; Kiefer, W. *Appl. Spectrosc.* **1990**, *44*, 776−782.

(34) Kiefer, W.; Bernstein, H. J. *Appl. Spectrosc.* **1971**, *25*, 500−501.

(35) Lauher, J. W.; Ibers, J. A. *J. Am. Chem. Soc.* **1973**, *95*, 5148−5152.

(36) Sato, S.; Aoyagi, K.; Haya, T.; Kitagawa, T. *J. Phys. Chem.* **1995**, *99*, 7766−7775.

(37) Koch, W.; Holthausen, M. C. *A Chemist's Guide to Density Functional Theory*; Wiley-VCH: Weinheim, Germany, 2000; pp 119−126.

(38) Nissum, M.; Funk, J.-M.; Kiefer, W. *J. Raman Spectrosc.* **1999**, *30*, 605−610.

(39) Mortensen, O. S.; Hassing, S. In *Advances in Infrared and Raman Spectroscopy*; Clark, R. J. H., Hester, R. E., Eds.; Heyden: London, 1980; Vol. 6, pp 1−60.